1 **Potential of next-generation imaging spectrometers to detect and quantify**

2 **methane point sources from space**

3 Daniel H. Cusworth[1,3], Daniel J. Jacob[1], Daniel J. Varon[1], Christopher Chan Miller[2], Xiong Liu[2], Kelly Chance[2],

4 Andrew K. Thorpe[3], Riley M. Duren[3], Charles E. Miller[3], David R. Thompson[3], Christian Frankenberg[3,4], Luis

5 Guanter[5], and Cynthia A. Randles[6]

6 [1]School of Engineering and Applied Sciences, Harvard University, Cambridge, MA, USA

7 [2]Atomic and Molecular Physics Division, Harvard Smithsonian Center for Astrophysics, Cambridge, MA, USA

8 [3]Jet Propulsion Laboratory, California Institute of Technology, Pasadena, CA, USA

9 [4]Division of Geology and Planetary Sciences, California Institute of Technology, Pasadena, CA, USA

10 [5]Centro de Tecnologías Físicas, Universitat Politècnica de València, Camí de Vera s/n, 46022 València, Spain

11 [6]ExxonMobil Research and Engineering Company, Annandale, NJ, USA

14 **Abstract**

15 We examine the potential for global detection of methane plumes from individual point sources with the new

16 generation of spaceborne imaging spectrometers (EnMAP, PRISMA, EMIT, SBG) scheduled for launch in 2019-2025.

17 These instruments are designed to map the Earth's surface with a sampling distance as fine as 30×30 m^2 but they have

18 spectral resolution of 7-10 nm in the 2200-2400 nm band that should also allow useful detection of atmospheric

19 methane. We simulate scenes viewed by EnMAP (10 nm spectral resolution, 180 signal-to-noise ratio) using the

20 EnMAP End-to-End Simulation Tool with superimposed methane plumes generated by large-eddy simulations. We

21 retrieve atmospheric methane and surface reflectivity for these scenes using the IMAP-DOAS optimal estimation

22 algorithm. We find an EnMAP precision of 4-13% for atmospheric methane depending on surface type, allowing

23 effective single-pass detection of 100+ kg h^{-1} methane point sources depending on surface brightness, surface

24 homogeneity, and wind speed. Successful retrievals over very heterogeneous surfaces such as an urban mosaic require

25 finer spectral resolution. We simulated the EnMAP capability with actual plume observations over oil/gas fields in

26 California from the airborne AVIRIS-NG sensor (3×3 m^2 pixel resolution, 5 nm spectral resolution, SNR 200-400).

27 We spectrally and spatially downsampled AVIRIS-NG images to match EnMAP instrument specifications and found

28 that we could successfully detect point sources of ~100 kg h^{-1} over bright surfaces. Estimated emission rates inferred

29 with a generic Integrated Mass Enhancement (IME) method agreed within a factor of 2 between EnMAP and AVIRIS-

30 NG. Better agreement may be achieved with a more customized IME method. Our results suggest that imaging

31   spectrometers in space could play a transformative role in the future for quantifying methane emissions from point

32   sources on a global scale.

33

34   **1 Introduction**

35   Methane is a powerful greenhouse gas, yet its sources are highly uncertain. Quantifying methane emissions

36   from different sources is critical for developing strategies to reduce atmospheric methane levels. Anthropogenic

37   emissions originate from a large number of point sources (coal mine vents, oil/gas facilities, livestock operations,

38   landfills, wastewater treatment plants) that are individually small, spatially clustered, often intermittent, and difficult to

39   quantify (Allen et al., 2013; Frankenberg et al., 2016). Here we investigate the unique potential of new-generation

40   satellite instruments designed to map the Earth's surface (imaging spectrometers) to also detect methane point sources

41   in the shortwave infrared (SWIR).

42   There has been considerable interest in using SWIR satellite observations of atmospheric methane columns by

43   solar backscatter to detect methane sources and test emission inventories (Jacob et al., 2016). These observations are

44   traditionally made by atmospheric sensors with high spectral resolution (<1 nm) to capture the fine structure of

45   methane absorption lines (Table 1). The requirement of high spectral resolution has generally implied a coarse pixel

46   resolution (>1 km) to achieve satisfactory signal-to-noise ratios (SNR), but this limits the ability to localize and

47   quantify individual point sources. Inverse analyses of observations from the SCIAMACHY instrument with 60 km

48   pixel resolution, and from the GOSAT instrument with sparse sampling at 10 km pixel resolution, have quantified

49   emissions over regional scales (Bergamaschi et al., 2009; Kort et al., 2014; Turner et al., 2015). The recently launched

50   TROPOMI instrument with global daily coverage at 7 km pixel resolution (Hu et al., 2018) will refine the regional

51   characterization but still cannot resolve point sources (Sheng et al., 2018). Planned instruments with ~1 km pixel

52   resolution (MethaneSat, Propp et al., 2017; Geo-FTS, Xi et al., 2016) should be able to detect large point sources after

53   inversion of several days of observations (Cusworth et al., 2018; Turner et al., 2018) but would not resolve densely

54   clustered or temporally variable sources.

55   Atmospheric sensors for methane generally focus on achieving high precision (<1%) and low relative bias

56   (<0.3%), appropriate for regional characterization of sources (Buchwitz et al., 2015). However, these requirements can

57   be relaxed if the focus is to observe individual plumes. Precision can be traded for pixel resolution because methane

58   plumes are generally sub-kilometer in scale (Frankenberg et al., 2016), so that plume enhancements are larger when the

59   pixel resolution is finer (Jacob et al., 2016). In a theoretical simulation study for the GHGSat microsatellite instrument

60   with 50×50 m^2 pixel resolution, Varon et al. (2018a) found that a 1-5% precision would be adequate for single-pass

61   observation of plumes to quantify point sources of magnitude ~100 kg h^{-1}. This would account for most of the total

62   methane emitted by point sources in the United States reporting to the Greenhouse Gases Reporting Program (Jacob et

63   al., 2016). A demonstration GHGSat instrument (GHGSat-D) launched in 2016 with an estimated precision of 13%

64   limited by instrument imperfections, has proven able to detect large point sources in excess of 1000 kg h^{-1} (Varon et al.,

65   2018b).

66   Here we examine the potential of a different class of satellite instruments, imaging spectrometers, to provide

67   global snapshots of individual methane point sources. These instruments are designed for global coverage of land

68   surfaces, but they may be used for atmospheric sensing as well. They have fine spatial sampling, or pixel resolution

69   (<100 m), with coarser spectral sampling to measure vibrational overtone absorptions in surface reflectance. Some

70   current imagers such as Landsat (Roy et al., 2014) and WorldView-3 (http://worldview3.digitalglobe.com) have

71   observing bands in the SWIR intended to infer soil moisture, mineral composition, and vegetation traits (Cleemput et

72   al., 2018). However, the SWIR spectral resolutions for Landsat (100 nm) and WorldView-3 (40-50 nm) are too coarse

73   to usefully observe methane. The Hyperion instrument onboard NASA Earth Observing-1 had 10 nm spectral

74   resolution in the SWIR but a very low signal to noise ratio (SNR) of 20 (Folkman et al., 2001).

75   A new generation of imaging spectrometers set for launch over the next few years (EnMAP, PRISMA, EMIT,

76   and an anticipated SBG investigation) will achieve ~10 nm or better spectral resolution in the SWIR with pixel

77   resolution in the range 30-60 m and SNR of 180-400 or beyond (Table 1). Experience with airborne imaging

78   spectrometers of comparable specifications suggests that these satellite instruments should be able to usefully observe

79   methane plumes. The Airborne Visible/Infrared Imaging Spectrometer (AVIRIS-C), with a 10 nm spectral resolution

80   and SNR of 70 (Green et al., 1998), was able together with Hyperion to detect the massive Aliso Canyon methane leak

81   in California (Thompson et al., 2016). The next generation AVIRIS instrument (AVIRIS-NG), with a finer spectral

82   resolution of 5 nm and SNR of 200 (Thorpe et al., 2014), was able to detect a range of methane plumes over the Four

83   Corners region of New Mexico including from gas processing facilities, storage tanks, pipeline leaks, well pads, and

84   coal mine venting shafts (Frankenberg et al., 2016). AVIRIS-NG was flown over 272000 potential methane emitting

85   facilities in California between 2016 and 2018 (CARB, 2017).

86

87   **2 Imaging spectrometer spectra including methane plumes**

88   The next generation of spaceborne imaging spectrometers in Table 1 includes PRISMA (launched March

89   2019), EnMAP (2020), EMIT (2022), SBG (2025-2027). The AMPS instrument (proposed) would bridge the gap

90   between surface imagers and methane sensors, by providing 1 nm SWIR spectral resolution while maintaining 30 m

91   spatial resolution (Thorpe et al., 2016). We will focus our baseline analysis on EnMAP, for which detailed

92   documentation is available (Guanter et al., 2015), and examine other instruments through sensitivity analyses. EnMAP

93   is a push-broom style instrument with 10 nm resolution in the SWIR and an expected 180 SNR at 2300 nm. PRISMA

94   (http://www.prisma-i.it/) has very similar instrument specifications as EnMAP. The EMIT instrument will fly on the

95   International Space Station. It is slated to have a 7-10 nm spectral resolution and 60 m pixel resolution (Green et al.,

96   2018). Other investigations, such as SBG, are called for in the NASA Earth Science and Applications Decadal Survey

97   (National Academies, 2018).

98   Figure 1 shows simulated transmission spectra in the weak (~1650 nm) and strong (~2300 nm) SWIR methane

99   absorption bands at the spectral resolutions of TROPOMI (0.25 nm FWHM), AVIRIS-NG (5 nm), and EnMAP (10

100   nm). EnMAP spectra are sampled following the precise wavelength positions given in Guanter et al. (2015). The 1650

101   nm methane band has the advantage of being near a CO_2 band, so that joint retrievals of methane and CO_2 can be

102   combined with independent knowledge of the CO_2 column mixing ratio to remove joint errors in surface reflectivity

103   and atmospheric scattering (the so-called "CO_2 proxy" method; Frankenberg et al. 2005a). However, the 1650 nm band

104   is much weaker than the 2300 nm band and only the 2ν Q-branch could be detected at coarser spectral resolution.

105   Sampling the transmission spectra at the EnMAP spectral resolution yields only 8 data points in the 1650 nm band as

106   compared to 25 in the 2300 nm band. The 2300 nm band also exhibits more resolved structure. Our early attempts to

107   use the CO_2 proxy method in the 1650 nm band with EnMAP synthetic spectra were unsuccessful. In what follows we

108   focus on the 2300 nm band as sampled in the useful 2210 - 2410 nm range.

109   We examined the sensitivity of EnMAP to atmospheric methane variability by generating synthetic top of

110   atmosphere (TOA) EnMAP scenes with variable methane over a variety of surface types. We used for this purpose the

111   EnMAP End-to-End Simulation Tool (EeteS; Segl, 2012), developed to generate EnMAP TOA spectra with expected

112   instrument error included. EeteS takes surface information from another imaging instrument (e.g., SPOT-5), and passes

113   the image through spatial, atmospheric, spectral, and radiometric modules to generate EnMAP spectra. The

114   atmospheric module is based on the MODTRAN5 radiative transfer code. It assumes a horizontally invariant 1800 ppb

115   dry air column methane mixing ratio (X_{CH4}) and here we add methane plumes simulated with the Weather and Research

116   Forecasting Model Large Eddy Simulation (WRF-LES) at 30×30 m^2 resolution (Varon et al., 2018a).

117   Figure 2 shows a simulated red-blue-green (RGB) EeteS image over Berlin. We consider four scenes within

118   this domain to add WRF-LES methane plumes and perform subsequent retrievals. The scenes - Grass, Dark (water),

119   Bright, Urban - have mean SWIR surface reflectances of 0.09, 0.02, 0.30, 0.13, respectively. The urban scene is highly

120   heterogeneous. The WRF-LES simulation is conducted with 30×30 m^2 resolution (the EnMAP pixel resolution), 100

121   W m^{-2} sensible heat flux (moderately unstable meteorological conditions), and a mean wind speed of 3.5 m s^{-1}. We

122   generate an ensemble of 15 instantaneous plumes by sampling the WRF-LES simulation at five time slices and for

123   three source rates of 100, 500, and 900 kg h^{-1}. This range is typical of large (but not unusually large) point sources

124   (Jacob et al., 2016).

125   We compute the optical depth of the methane plume $\tau(\lambda)$ at wavelength λ by multiplying HITRAN absorption

126   cross sections (σ_H; Kochanov et al., 2016) by the methane mixing ratio enhancement (ΔVMR) and density of dry air

127   (VCD) in the 72-layered atmosphere of the MERRA-2 meteorological reanalysis (Gelaro et al., 2017):

128
$$\tau(\lambda) = \sum_{i=1}^{72} \Delta VMR_i \, VCD_i \, \sigma_{H,i}(\lambda). \quad (1)$$

129

130   The plume transmission $T(\lambda)$ is the negative exponential of $\tau(\lambda)$ weighted by the geometric airmass factor A (AMF) for

131   the backscattered solar radiation:

132

133
$$T(\lambda) = \exp\{-A\tau(\lambda)\}. \quad (2)$$

134

135   Each pixel's EeteS radiance spectrum is multiplied by this additional plume transmission. We do not add noise or

136   aerosol effects to the plume transmission spectra because the EeteS scene already accounts for those in the computation

137   of back-scattered radiances, and the plume transmission is just a multiplicative factor on these back-scattered radiances.

138   Figure 3 shows an example WRF-LES plume (500 kg h^{-1} source rate) superimposed over the Grass and Urban scenes.

139   EnMAP has a specific spectral resolution and SNR. We examined the sensitivity of the retrieval to these

140   parameters by generating synthetic spectra for different spectral resolutions and SNRs, thus extending our analysis to

141   other new-generation imaging spectrometers (Table 1). For this purpose, we interpolated EeteS surface radiance spectra

142   to the desired spectral resolution assuming no instrument noise. We then multiplied these radiance spectra by the

143   standard atmosphere plus WRF-LES plume transmission spectra and added uncorrelated instrument noise as per the

144   specified SNR.

145   To test our EnMAP retrievals on actual data, we also downsampled AVIRIS-NG images taken from aircraft

146   over California (CARB, 2017) to match EnMAP spatial resolution, and further convolved these spectra with a 10 nm

147   Gaussian filter to match EnMAP spectral resolution and wavelength positions. AVIRIS-NG flew at 3-4 km above the

148   ground, so we simulated additional extinction at higher altitudes based on the U.S standard atmosphere (Kneizys et al.,

149   1996). We compared the retrieved methane from AVIRIS-NG and the synthetic EnMAP to determine the ability of

150   EnMAP to detect and quantify the methane point sources identified by AVIRIS-NG.

151

152   **3 Methane retrieval**

153   We retrieved methane from the synthetic imaging spectrometer spectra by adapting the Iterative Maximum A

154   Posteriori - Differential Optical Absorption Spectroscopy (IMAP-DOAS) algorithm developed for AVIRIS

155   (Frankenberg et al., 2005b; Thorpe et al., 2017; Ayasse et al., 2018). DOAS retrievals isolate higher frequency features

156   resulting from gas absorption from lower frequency features that include surface reflectance as well as Rayleigh and

157   Mie scattering (Bovensmann et al., 2011). A polynomial term accounts for the low frequency features (Thorpe et al.,

158   2017).

159

160   *3.1 State vector*

161   In addition to methane (CH_4), the retrieval must account for variable absorption by water vapor (H_2O) and

162   nitrous oxide (N_2O) over the 2210-2400 nm spectral region. We parameterize low frequency spectroscopic features as a

163   sum of Legendre polynomials of order $k = [0, K]$ with coefficients a_k. The state vector ($\mathbf{x}$) optimized through the

164   retrieval is therefore composed of the following elements:

$$\mathbf{x} = (s_{CH4}, s_{H2O}, s_{N2O}, a_0, \ldots, a_K)$$

166   where s is a scaling factor applied to the column mixing ratio of each gas from the U.S standard atmosphere (Kneizys et

167   al., 1996). We do not include aerosols in the retrieval as they play little role at the relevant spatial and spectral

168   resolution (Ayasse et al., 2018). Methane point sources generally do not co-emit aerosols.

169

170   *3.2 Optimal estimation*

171   To retrieve the state vector from the Eetes TOA radiances, we use a forward model similar to previous IMAP-

172   DOAS algorithms (Thorpe et al., 2017, Ayasse et al., 2018), with a modification to the polynomial term for surface

173   reflectance:

174
$$F^h(\mathbf{x},\lambda) = I_0(\lambda) \exp\left(-A \sum_{n=1}^{3} s_n \sum_{l=1}^{72} \tau_{n,l}\right) \sum_{k=0}^{K} a_k P_k(\lambda) \quad (3)$$

175 Here F^h is the high-resolution backscattered TOA radiance at wavelength λ, $I_0(\lambda)$ is the incident TOA solar intensity,

176 $\tau_{n,l}$ is the default optical depth from the US standard atmosphere for trace gas element $n = [1,3]$ of the state vector at

177 vertical level $l = [1,72]$, s_n is the scaling factor to that default optical depth optimized in the retrieval, $P_k(\lambda)$ is the kth

178 Legendre polynomial, and the a_k are coefficients optimized in the retrieval. The optical depth $\tau_{n,l}$ is computed in the

179 same fashion as Equation 1, using information from the MERRA-2 reanalysis and HITRAN absorption cross sections.

180 For satellite retrievals, the AMF is a scalar describing the optical path through the atmosphere. In Section 4.3, we apply

181 the IMAP-DOAS algorithm to airborne AVIRIS-NG scenes and use a vector-valued AMF that depends on the height of

182 the aircraft.

183 Previous IMAP-DOAS algorithms used a simple polynomial approximation for the surface reflectance, but

184 here we use Legendre polynomials to exploit their orthogonality. We find that $K = 4$ provides sufficient spectral

185 resolution whereas previous applications using simple polynomials required $K = 6$ (Ayasse et al., 2018).

186 We compute the TOA backscattered radiances $F^h(\mathbf{x},\lambda)$ over the 2210-2410 nm spectral range at 0.02 nm

187 resolution, and assemble these in a vector $\mathbf{F}^h(\mathbf{x})$ representing the high-resolution spectrum as simulated by the forward

188 model for a given $\mathbf{x}$. We convolve this spectrum with the instrument FWHM and then sample at the known wavelength

189 positions. For example, for EnMAP, we convolve $\mathbf{F}^h(\mathbf{x})$ with a 10 nm FWHM and sample the resulting spectra at

190 EnMAP's 10 nm intervals to get the low-resolution $\mathbf{F}(\mathbf{x})$. We also explored performing separate convolutions on the

191 high resolution transmission and polynomial terms in Equation 3, and then multiplying them together to get $\mathbf{F}(\mathbf{x})$. We

192 found little difference in the results between methods.

193 Observed backscattered TOA radiances ($\mathbf{y}$) can be represented as

194
$$\mathbf{y} = \mathbf{F}(\mathbf{x}) + \boldsymbol{\epsilon} \quad (4)$$

195 where the observational error $\boldsymbol{\epsilon}$ is the sum of instrument and forward model errors. As is commonly done for satellite

196 retrievals, we assume that the forward model error is small compared to the instrument error characterized by the SNR.

197 The forward model is non-linear so that the solution must be obtained iteratively. A Jacobian matrix is calculated for

198 each iteration of the state vector

199
$$\mathbf{K}_i = \left.\frac{\partial \mathbf{F}}{\partial \mathbf{x}}\right|_{\mathbf{x}=\mathbf{x_i}} \quad (5)$$

200 and we employ a Gauss-Newton iteration to solve iteratively for the optimal state vector (Rodgers, 2000):

201 $$\mathbf{x}_{i+1} = \mathbf{x}_A + (\mathbf{K}_i^T \mathbf{S}_O^{-1} \mathbf{K}_i + \mathbf{S}_A^{-1})^{-1} \mathbf{K}_i^T \mathbf{S}_O^{-1} [y - \mathbf{F}(\mathbf{x}_i) + \mathbf{K}_i(\mathbf{x}_i - \mathbf{x}_A)] \quad (6)$$

202 Here $\mathbf{S}_O = [\boldsymbol{\varepsilon}\boldsymbol{\varepsilon}^T]$ is the observation error covariance matrix defined by the instrument SNR, $\mathbf{x}_A$ is the prior estimate of the

203 state vector, and $\mathbf{S}_A$ is the prior error covariance matrix. We set a weak prior error variance for methane, $\sigma_{s_{CH4}}^2 = 5$, to

204 accommodate large plume enhancements. The prior X_{CH4} estimate is 1800 ppb. The iterative analytical solution to the

205 inverse problem as described by equation (6) also provides the posterior error covariance matrix ($\hat{\mathbf{S}}$) as part of the

206 solution:

207 $$\hat{\mathbf{S}} = \left(\mathbf{K}_i^T \mathbf{S}_O^{-1} \mathbf{K}_i + \mathbf{S}_A^{-1}\right)^{-1} \quad (7)$$

208

209 $\hat{\mathbf{S}}$ gives information on the error correlation between retrieved methane and surface reflectivity, which is a major

210 concern for methane retrievals (Butz et al., 2012).

211

212 **4. Results and Discussion**

213 *4.1 EnMAP plume retrievals over different surfaces*

214   Figure 3 shows examples of the IMAP-DOAS retrievals of 500 kg h^{-1} and 900 kg h^{-1} WRF-LES plumes over

215 the Grass and Urban scenes. Near the emission source, the 500 kg h^{-1} plume is clearly defined in the Grass scene. It is

216 also detectable in the Urban scene but obscured by surface retrieval artifacts. The 900 kg h^{-1} plume is better captured

217 over both surfaces, though major retrieval artifacts remain in the Urban scene.

218   Varon et al. (2018a) previously estimated the theoretical ability of a satellite instrument to quantify source

219 rates from point sources as a function of instrument precision, assuming a uniform surface reflectance. They concluded

220 that an instrument with 1-5% precision on X_{CH4} would be able to quantify point sources with an error of 70-170 kg h^{-1}.

221 Here we characterize the EnMAP instrument precision as the relative root-mean squared-error (RRMSE) between the

222 true and retrieved column methane concentrations for individual 30×30 m^2 pixels in the scenes of Figure 2 including

223 the WRF-LES plumes. Figure 4 summarizes the results for the four scenes of Figure 2. We find precisions of 8.2 ±

224 0.7% for Grass, 13 ± 0.7% for Urban, and 3.7 ± 0.5% for Bright scenes. The standard deviations refer to the RRMSEs

225 computed for the 15 different realizations of the WRF-LES plumes and for the 3 source rates of 100, 500, and 900 kg h[-]

226 [1]. The Dark scene was consistently unsuccessful, with error of at least 100% for each realization, and we do not discuss

227 it further. The Bright scene performs the best because of the large backscattered photon flux. The Urban scene performs

228 worse than the Grass scene, even though its average SWIR surface reflectance is larger, due to the larger variability in

229 reflectance over the scene including dark pixels. As illustrated in Figure 3, the 8% precision over the relatively uniform

230 grass surface should enable EnMAP to successfully quantify 500 kg h^{-1} point sources in a single pass.

231   Beyond the precision for the methane retrieval, an additional limitation for retrieving point sources is the error

232 correlation with variable surface reflectance. This is illustrated in Figure 3 with the retrieved X_{CH4} enhancements over

233 Grass and Urban scenes relative to the background. In the case of the Grass scene with a 500 kg h^{-1} source, the 8%

234 precision limits the ability to observe the downwind plume but there is a clear enhancement over background at the

235 source location. With a 900 kg h^{-1} source the downwind plume becomes well-defined against the background. In the

236 case of the Urban scene, the detection of the 500 kg h^{-1} plume is far more problematic because of large positive artifacts

237 over dark (water) pixels. The 900 kg h^{-1} plume is still difficult to distinguish from the artifacts and would require prior

238 knowledge of source location to be identified and quantified. The error correlation between methane and surface

239 reflectance in the retrieval can be reduced by increasing the spectral resolution of the instrument as discussed in Section

240 4.2.

241

242 *4.2 Sensitivity to instrument spectral resolution and SNR*

243   Here we examine the potential of future instruments with improved spectral resolution and SNR relative to

244 EnMAP (Table 1) to achieve improved retrievals of point sources. Figure 5 shows the change in retrieval precision as

245 we vary the spectral resolution from 10 to 1 nm and the SNR from 100 to 500. The precision estimates are calculated

246 using two methods. First, we estimate the precision by evaluating the RRMSEs averaged over the Grass, Urban, and

247 Bright scenes of Figure 2, for 3 source rates and 15 instantaneous plume realizations, following the procedure of

248 Section 4.1. Since SNR varies on a per-pixel basis, the plotted SNRs for this method represent the mean scene SNR.

249 Specifications of the instruments in Table 1 are identified on the plot. Precision improves as spectral resolution and

250 SNR increase, as expected. The dependencies are not linear, and the contours are concave, meaning that precision is

251 more effectively improved by increasing spectral resolution by a certain factor than by increasing SNR by the same

252 factor. Increasing the spectral resolution improves precision through multiple independent factors: by increasing the

253 number of independent measurements across the methane interval; by increasing the effective squared depth of the

254 sharpest methane absorptions, for improved spectral contrast relative to the continuum; and by better resolution of the

255 unique methane absorption shape, which improves discrimination against potential surface confusers.

256   Second, we estimate theoretical precision in Figure 5 by extracting the associated X_{CH4} posterior error

257 covariance term of $\hat{S}$ from Equation 7. Here we find that instrument precision improves more as a function of SNR than

258   spectral resolution, which is a different result than the first precision method. Issues with the surface retrieval drive the

259   contrasting results between the two methods. This underscores the difficulty in assigning a single retrieved X_{CH4}

260   uncertainty value for different instrument configurations. For a spaceborne AVIRIS-NG instrument, multiple along-

261   track samples would increase the SNR as a function of $\sqrt{N}$, where N = number of along-track frames. For the second

262   precision method, doing multiple along-track samples improves the theoretical precision from 5% to 1%. Varon et al.

263   (2018a) found that an instrument with 5% precision could constrain most anthropogenic point sources above 170 kg h^{-1}.

264   Using both the RRMSE and theoretical precision methods of Figure 5, we find that a spaceborne AVIRIS-NG

265   instrument (spectral resolution 5 nm, SNR 200-400) would have a precision of 5.5 − 1.0%, meaning that such an

266   instrument could constrain a majority of anthropogenic methane point sources.

267   A benefit of increasing spectral resolution is to improve decoupling of surface and methane spectroscopic

268   features. We saw in Figure 3 that this was a major source of error over inhomogeneous surfaces such as the Urban

269   scene. It is manifested in the retrieval by an error correlation between state vector elements s_{CH4} (scaling factor for

270   methane column mixing ratios) and a_k (coefficients for the surface reflectivity described by Legendre polynomials).

271   This error correlation is described by the posterior error covariance matrix $\hat{\mathbf{S}}$ obtained as part of the retrieval (Equation

272   6). For example, the error correlation decreases significantly between EnMAP (r = -0.33) and AMPS (r = -0.19). This

273   driven by the increase in spectral resolution from 10 nm to 1 nm. A separate test shows that simply increasing the SNR

274   to 300 (as for SBG) does not improve the error correlation.

275   An important implication of decoupling X_{CH4} from the surface reflectance in the retrieval is to improve the

276   capability for plume pattern recognition, which is necessary to convert observed plume methane enhancements into

277   source rates (Varon et al., 2018a). Figure 6 illustrates this for the Grass and Urban scenes of Figure 3 including the

278   plume from the 500 kg h^{-1} point source. Following Varon et al. (2018a), we define the plume for the retrieved scenes

279   ==with a plume mask that applies median and Gaussian filters to pixels above the 80th percentile of X_{CH4} within the scene.==

280   Retrievals are performed with the specifications of the EnMAP instrument (10 nm spectral resolution, SNR 180), SBG

281   (10 nm, 300), and AMPS (1 nm, 400).

282   For the Grass scene we find that all three instruments can discern the plume pattern near the emission source

283   and separate it from surface features. SBG and AMPS capture larger plume domains because of their higher precisions

284   (Figure 5), ==but a source rate can still be estimated successfully with EnMAP== by taking into account the dependence of

285   the retrieved plume extent on instrument precision (Varon et al., 2018a). For the Urban scene, EnMAP plume detection

286   is swamped by surface artifacts. Simply increasing the SNR as in the SBG instrument does not improve the situation.

287   Increasing the spectral resolution to 1 nm as in the AMPS instrument enables detection of the plume though

288   quantification would still be prone to surface artifacts.

289

290   *4.3 Evaluation with AVIRIS-NG observations*

291   To test the EnMAP retrieval capability with actual observations, we downsampled AVIRIS-NG spectra taken

292   over California methane emitting facilities (CARB, 2017). We chose three scenes observed by AVIRIS-NG on

293   different days over oil and gas facilities. Figure 7 shows the RGB images, the AVIRIS-NG plume retrievals performed

294   by applying the method of Section 3 with a variable AMF, and the downsampled EnMAP retrievals. Plume masks

295   have been applied in the same way as for Figure 6. At the altitudes used for the California survey, AVIRIS-NG has 3×3

296   m^2 pixel resolution and hence features much sharper methane enhancements than EnMAP (note the different scales for

297   the middle and right panels).

298   We see from Figure 7 that EnMAP is able to detect the same plumes as AVIRIS-NG (two plumes in the

299   bottom panels). This is facilitated by the brightness of the surfaces. The surface reflectivities retrieved simultaneously

300   with the methane enhancements in our IMAP-DOAS algorithm are 0.39-0.49, brighter than the Bright EeteS scene in

301   Section 4.1.

302   The plume observations can be related to the corresponding source rates by computing the integrated mass

303   enhancements (IME) within the plume mask (Frankenberg et al., 2016; Varon et al., 2018a). The IME is calculated as:

304    $$IME = \sum_{i=1}^{N} \Delta\Omega_i \Lambda_i \quad (7)$$

305   where $\Delta\Omega_i$ is the plume mass enhancement in pixel i relative to background (kg m^{-2}), Λ_i is the corresponding area of

306   the pixel, and the summation is over the N pixels within the plume mask. The point source rate Q is then inferred from

307   the IME as (Varon et al., 2018a)

308    $$Q = \frac{U_{eff}}{L} IME \quad (8)$$

309   where $L = \sqrt{\sum_{i=1}^{N} \Lambda_i}$ is a characteristic plume size and U_{eff} is an effective wind speed describing the rate of turbulent

310   dissipation of the plume (L/U_{eff} is the lifetime of the plume against turbulent dissipation to below the detection limit).

311   Varon et al. (2018a) relate U_{eff} to the 10-m wind speed (U_{10}) by fitting to WRF-LES simulations. Here we use their

312   relationship derived for the a 50 m pixel resolution, 5% precision instrument (Varon et al., 2018), and apply it as a

313   rough approximation to the AVIRIS-NG and downsampled EnMAP plumes:

314    $$U_{eff} = 1.1 \log U_{10} + 0.6 \quad (9)$$

315   where U_{eff} and U_{10} are in units of [m s^{-1}]. We obtain U_{10} from the HRRR-Reanalysis at 3-km hourly resolution

316   (https://rapidrefresh.noaa.gov/).

317   Figure 7 shows the source rates inferred from the AVIRIS-NG and EnMAP retrievals for each point source.

318   The AVIRIS-NG source rates are a factor of 1.2-3.0 greater (average 1.9) than the EnMAP source rates. There could be

319   several factors behind this discrepancy including error correlation with surface reflectivity in the EnMAP retrieval that

320   would cause some loss of the plume, and use of a generic plume mask and IME algorithm for both instruments. As

321   pointed out by Varon et al. (2018a), the U_{10}-U_{eff} relationship needs to be tailored to the pixel resolution and precision of

322   the particular instrument, and to the choice of plume mask. Nevertheless, the results do confirm that EnMAP should be

323   able to detect plumes and quantify source rates down to ~100 kg h^{-1} when the scene is sufficiently bright.

324

325   **5 Conclusions**

326   We examined the potential of next-generation spaceborne imaging spectrometers (EnMAP, PRISMA, EMIT,

327   SBG,) for observing atmospheric methane plumes from point sources and inferring the corresponding source rates.

328   These instruments have launch dates of 2019-2025 and focus on observing the Earth surface with fine pixel resolution

329   (30 × 30 m^2), but they also have observing channels at 2200-2400 nm with 7-10 nm spectral resolution that could be

330   used to retrieve methane plumes. This would achieve much finer spatial resolution than the standard satellite

331   instruments designed to measure atmospheric methane, and would provide a unique resource for global mapping of

332   individual methane point sources.

333   We focused our baseline analysis on EnMAP (spectral resolution 10 nm, SNR 180, 2020 launch date) as its

334   specifications are well documented (Guanter et al, 2015). We created synthetic spectra using the EnMAP End-to-End

335   Simulation Tool (EeteS) to simulate various surface scenes (Grass, Urban, Bright) with instrument errors and with

336   superimposed methane plumes generated by a WRF Large Eddy Simulation (LES). We then retrieved these scenes for

337   atmospheric methane together with surface reflectivities using the Iterative Maximum A Posteriori - Differential

338   Optical Absorption Spectroscopy (IMAP-DOAS) approach. The resulting precisions for methane are 8% for the Grass

339   scene, 13% for Urban, and 4% for Bright. A 500 kg h^{-1} methane plume (typical of very large point sources) is readily

340   detected over the relatively homogeneous Grass surface. The highly heterogeneous Urban surface is much more

341   challenging because of retrieval artifacts.

342   The limitation of EnMAP in detecting methane plumes over heterogeneous surfaces is caused by error

343   correlation between methane and surface reflectivity in the retrieval. We examined how precision and error correlation

344 could be improved by increasing spectral resolution and SNR. We find that spectral resolution reduces error

345 correlation more important than SNR. The proposed Atmospheric Methane Plume Spectrometer (AMPS), which

346 bridges the gap between imaging spectrometers and atmospheric sensors (1 nm spectral resolution, SNR 400), can

347 greatly decrease surface artifacts and detect a 500 kg h^{-1} plume even over the heterogeneous Urban surface. Alternative

348 surface parameterizations might also improve X_{CH4} and surface separation. For example, a channelwise representation

349 with reflectances tied through an empirical covariance structure (Thompson et al., 2018) has been used previously to

350 improve consistency in water vapor estimations. Alternative algorithms, such as matched filter approaches (Ong et al.,

351 2019) may show different X_{CH4} sensitivities, and in particular may be better able to represent structured reflectances of

352 more complex surfaces.

353   We tested the EnMAP capability with actual observations by downsampling AVIRIS-NG images taken from

354 aircraft (3 × 3 m^2 pixels, 5 nm spectral resolution, SNR 200) over California methane emitting facilities (CARB, 2017).

355 We showed that these EnMAP-like images are able to detect and quantify actual plumes of magnitude ~100 kg h^{-1} over

356 relatively bright surfaces. Source rates inferred from the plumes with a generic Integrated Mass Enhancement (IME)

357 method are a factor of 1.2 to 3 lower for EnMAP than for AVIRIS-NG, which could be due in part to unaccounted

358 dependence of the IME method on instrument pixel size and precision.

359   In summary, our analysis shows that future spaceborne imaging spectrometers designed to map the Earth

360 surface in the SWIR also have considerable potential for detecting methane plumes from point sources and quantifying

361 source rates. The detection capability of 100-500 kg h^{-1} over relatively bright or homogeneous land surfaces would

362 allow accounting for a wide range of point sources. The fine spatial resolution of these instruments should make them a

363 unique resource to contribute to tiered observing systems for greenhouse gases (Duren and Miller, 2012).

364

365 **Acknowledgments**. This work was supported in part by the ExxonMobil Research and Engineering Company and

366 NASA's Carbon Monitoring System (CMS) Prototype Methane Monitoring System for California. Data from the

367 California Methane Survey was supported by NASA's Earth Science Division, the California Air Resources Board

368 under ARB-NASA Agreement 15RD028 Space Act Agreement 82-19863 and the California Energy Commission

369 under CEC-500-15-004. Portions of this work was undertaken at the Jet Propulsion Laboratory, California Institute of

370 Technology, under contract with NASA

References

Allen, D. T., Torres, V. M., Thomas, J., Sullivan, D. W., Harrison, M., Hendler, A., Herndon, S. C., Kolb, C. E., Fraser, M. P., Hill, A. D., Lamb, B. K., Miskimins, J., Sawyer, R. F., and Seinfeld, J. H.: Measurements of methane emissions at natural gas production sites in the United States, Proceedings of the National Academy of Sciences, 110, 17 768–17 773, doi:10.1073/pnas.1304880110, URL https://www.pnas.org/content/110/44/17768, 2013.

Ayasse, A. K., Thorpe, A. K., Roberts, D. A., Funk, C. C., Dennison, P. E., Frankenberg, C., Steffke, A., and Aubrey, A. D.: Evaluating the effects of surface properties on methane retrievals using a synthetic airborne visible/infrared imaging spectrometer next generation (AVIRIS-NG) image, Remote Sensing of Environment, 215, 386 – 397, doi:https://doi. org/10.1016/j.rse.2018.06.018, URL http://www.sciencedirect.com/science/article/ pii/S0034425718302967, 2018.

Bergamaschi, P., Frankenberg, C., Meirink, J. F., Krol, M., Villani, M. G., Houweling, S., Dentener, F., Dlugokencky, E. J., Miller, J. B., Gatti, L. V., Engel, A., and Levin, I.: Inverse modeling of global and regional CH4 emissions using SCIAMACHY satellite retrievals, Journal of Geophysical Research: Atmospheres, 114, doi:10.1029/2009JD012287, URL https://agupubs.onlinelibrary.wiley.com/doi/abs/10.1029/2009JD012287, 2009.

Bovensmann, H., Doicu, A., Stammes, P., Van Roozendael, M., Von Savigny, C., de Vries, M. P., Beirle, S., Wagner, T., Chance, K., Buchwitz, M., et al.: From Radiation Fields to Atmospheric Concentrations–Retrieval of Geophysical Parameters, in: SCIAMACHY-Exploring the Changing Earth's Atmosphere, pp. 99–127, Springer, 2011.

Buchwitz, M., Reuter, M., Schneising, O., Boesch, H., Guerlet, S., Dils, B., Aben, I., Armante, R., Bergamaschi, P., Blumenstock, T., Bovensmann, H., Brunner, D., Buchmann, B., Burrows, J., Butz, A., Che´din, A., Chevallier, F., Crevoisier, C., Deutscher, N., Frankenberg, C., Hase, F., Hasekamp, O., Heymann, J., Kaminski, T., Laeng, A., Lichtenberg, G., Mazie`re, M. D., Noe¨l, S., Notholt, J., Orphal, J., Popp, C., Parker, R., Scholze, M., Sussmann, R., Stiller, G., Warneke, T., Zehner, C., Bril, A., Crisp, D., Griffith, D., Kuze, A., O'Dell, C., Oshchepkov, S., Sherlock, V., Suto, H., Wennberg, P., Wunch, D., Yokota, T., and Yoshida, Y.: The Greenhouse Gas Climate Change Initiative (GHG-CCI): Comparison and quality assessment of near-surface-sensitive satellite-derived CO2 and CH4 global data sets, Remote Sensing of Environment, 162, 344 – 362, doi:https://doi.org/10.1016/j.rse.2013.04.024, URL http://www.sciencedirect.com/science/article/pii/S0034425713003520, 2015.

Butz, A., Galli, A., Hasekamp, O., Landgraf, J., Tol, P., and Aben, I.: TROPOMI aboard Sentinel-5 Precursor: Prospective performance of CH4 retrievals for aerosol and cirrus loaded atmospheres, Remote Sensing of Environment, 120, 267 – 276, doi:https://doi.org/10.1016/j.rse.2011.05.030, URL http://www.sciencedirect.com/science/article/pii/S003442571200082X, the Sentinel Missions

- New Opportunities for Science, 2012.

CARB: Introduction to the Phase I Report of the California Methane Survey from the Staff of the California Air Resources Board (CARB), Tech. rep., The California Air Resources Board, URL: https://ww3.arb.ca.gov/research/methane/ca_ch4_survey_phase1_report_2017.
5   pdf?_ga=2.259065807.470178342.1556320978-319883758.1556320978, 2017.

Cleemput, E. V., Vanierschot, L., Ferna´ndez-Castilla, B., Honnay, O., and Somers, B.: The functional characterization of grass- and shrubland ecosystems using hyperspectral remote sensing: trends, accuracy and moderating variables, Remote Sensing of Environment, 209, 747 – 763, doi:https://doi.org/10.1016/j.rse.2018.02.030, URL http://www.sciencedirect.com/
10   science/article/pii/S0034425718300427, 2018.

Cusworth, D. H., Jacob, D. J., Sheng, J.-X., Benmergui, J., Turner, A. J., Brandman, J., White, L., and Randles, C. A.: Detecting high-emitting methane sources in oil/gas fields using satellite observations, Atmospheric Chemistry and Physics, 18, 16 885–16 896, doi:10.5194/ acp-18-16885-2018, URL https://www.atmos-chem-phys.net/18/16885/2018/, 2018.

15 Duren, R. M. and Miller, C. E.: Measuring the carbon emissions of megacities, Nature Climate Change, 2, 560, 2012.

Folkman, M. A., Pearlman, J., Liao, L. B., and Jarecke, P. J.: EO-1/Hyperion hyperspectral imager design, development, characterization, and calibration, in: Hyperspectral Remote Sensing of the Land and Atmosphere, vol. 4151, pp. 40–52, International Society for Optics and Photonics, 2001.

20 Frankenberg, C., Meirink, J. F., van Weele, M., Platt, U., and Wagner, T.: Assessing Methane Emissions from Global Space-Borne Observations, Science, 308, 1010–1014, doi:10. 1126/science.1106644, URL http://science.sciencemag.org/content/308/5724/1010, 2005.

Frankenberg, C., Platt, U., and Wagner, T.: Iterative maximum a posteriori (IMAP)-DOAS for retrieval of strongly absorbing trace gases: Model studies for CH4 and CO2 retrieval from near
25   infrared spectra of SCIAMACHY onboard ENVISAT, Atmospheric Chemistry and Physics, 5, 9–22, doi:10.5194/acp-5-9-2005, URL https://www.atmos-chem-phys.net/5/9/2005/, 2005b.

Frankenberg, C., Meirink, J., Bergamaschi, P., Goede, A., Heimann, M., Ko¨rner, S., Platt, U., van Weele, M., and Wagner, T.: Satellite chartography of atmospheric methane from SCIAMACHY on board ENVISAT: Analysis of the years 2003 and 2004, Journal of Geophysical Research:
30   Atmospheres, 111, 2006.

Frankenberg, C., Thorpe, A. K., Thompson, D. R., Hulley, G., Kort, E. A., Vance, N., Borchardt, J., Krings, T., Gerilowski, K., Sweeney, C., Conley, S., Bue, B. D., Aubrey, A. D., Hook, S., and Green, R. O.: Airborne methane remote measurements reveal heavy-tail flux distribution in Four Corners region, Proceedings of the National Academy of Sciences, 113, 9734–9739,

doi:10.1073/pnas.1605617113, URL https://www.pnas.org/content/113/35/9734, 2016.

Gelaro, R., McCarty, W., Sua´rez, M. J., Todling, R., Molod, A., Takacs, L., Randles, C. A., Darmenov, A., Bosilovich, M. G., Reichle, R., Wargan, K., Coy, L., Cullather, R., Draper, C., Akella, S., Buchard, V., Conaty, A., da Silva, A. M., Gu, W., Kim, G.-K., Koster, R., Lucchesi, R., Merkova, D., Nielsen, J. E., Partyka, G., Pawson, S., Putman, W., Rienecker, M., Schubert, S. D., Sienkiewicz, M., and Zhao, B.: The Modern-Era Retrospective Analysis for Research and Applications, Version 2 (MERRA-2), Journal of Climate, 30, 5419–5454, doi:10.1175/ JCLI-D-16-0758.1, URL https://doi.org/10.1175/JCLI-D-16-0758.1, 2017.

Green, R., Mahowald, N., Clark, R., Ehlmann, B., Ginoux, P., Kalashnikova, O., Miller, R., Okin, G., Painter, T., Pe´rez Garc´ıa-Pando, C., et al.: NASA's Earth Surface Mineral Dust Source Investigation, in: AGU Fall Meeting Abstracts, 2018.

Green, R. O., Eastwood, M. L., Sarture, C. M., Chrien, T. G., Aronsson, M., Chippendale, B. J., Faust, J. A., Pavri, B. E., Chovit, C. J., Solis, M., Olah, M. R., and Williams, O.: Imaging Spectroscopy and the Airborne Visible/Infrared Imaging Spectrometer (AVIRIS), Remote Sensing of Environment, 65, 227 – 248, doi:https://doi.org/10.1016/ S0034-4257(98)00064-9, URL http://www.sciencedirect.com/science/article/pii/ S0034425798000649, 1998.

Guanter, L., Kaufmann, H., Segl, K., Foerster, S., Rogass, C., Chabrillat, S., Kuester, T., Hollstein, A., Rossner, G., Chlebek, C., Straif, C., Fischer, S., Schrader, S., Storch, T., Heiden, U., Mueller, A., Bachmann, M., Mu¨hle, H., Mu¨ller, R., Habermeyer, M., Ohndorf, A., Hill, J., Buddenbaum, H., Hostert, P., Van der Linden, S., Leita˜o, P. J., Rabe, A., Doerffer, R., Krasemann, H., Xi, H., Mauser, W., Hank, T., Locherer, M., Rast, M., Staenz, K., and Sang, B.: The EnMAP Spaceborne Imaging Spectroscopy Mission for Earth Observation, Remote Sensing, 7, 8830–8857, doi:10.3390/rs70708830, URL http://www.mdpi.com/2072-4292/7/7/8830, 2015.

Hochberg, E. J., Roberts, D. A., Dennison, P. E., and Hulley, G. C.: Special issue on the Hyperspectral Infrared Imager (HyspIRI): Emerging science in terrestrial and aquatic ecology, radiation balance and hazards, Remote Sensing of Environment, 167, 1 – 5, doi:https://doi. org/10.1016/j.rse.2015.06.011, URL http://www.sciencedirect.com/science/article/ pii/S0034425715300420, special Issue on the Hyperspectral Infrared Imager (HyspIRI), 2015.

Hu, H., Landgraf, J., Detmers, R., Borsdorff, T., Aan de Brugh, J., Aben, I., Butz, A., and Hasekamp, O.: Toward Global Mapping of Methane With TROPOMI: First Results and Intersatellite Comparison to GOSAT, Geophysical Research Letters, 45, 3682–3689, doi:10. 1002/2018GL077259, URL https://agupubs.onlinelibrary.wiley.com/doi/abs/10. 1002/2018GL077259, 2018.

Jacob, D. J., Turner, A. J., Maasakkers, J. D., Sheng, J., Sun, K., Liu, X., Chance, K., Aben, I., McKeever, J., and Frankenberg, C.: Satellite observations of atmospheric methane and their value for quantifying methane emissions, Atmospheric Chemistry and Physics, 16, 14 371–14 396,

doi:10.5194/acp-16-14371-2016, URL https://www.atmos-chem-phys.net/16/14371/2016/, 2016.

Kneizys, F., Abreu, L., Anderson, G., Chetwynd, J., Shettle, E., Berk, A., Bernstein, L., Robertson, D., Acharya, P., and Rothman, L.: The MODTRAN 2/3 report and LOWTRAN 7 model, Phillips Laboratory, Hanscom AFB, MA, 1731, 1996.

Kochanov, R., Gordon, I., Rothman, L., Wcisło, P., Hill, C., and Wilzewski, J.: HITRAN Application Programming Interface (HAPI): A comprehensive approach to working withspectroscopic data, Journal of Quantitative Spectroscopy and Radiative Transfer, 177, 15–30, doi:https://doi.org/10.1016/j.jqsrt.2016.03.005, URL http://www.sciencedirect.com/science/article/pii/S0022407315302466, xVIIIth Symposium on High Resolution Molecular Spectroscopy (HighRus-2015), Tomsk, Russia, 2016.

Kort, E. A., Frankenberg, C., Costigan, K. R., Lindenmaier, R., Dubey, M. K., and Wunch, D.: Four corners: The largest US methane anomaly viewed from space, Geophysical Research Letters, 41, 6898–6903, doi:10.1002/2014GL061503, URL https://agupubs.onlinelibrary.wiley.com/doi/abs/10.1002/2014GL061503, 2014.

Kuze, A., Suto, H., Shiomi, K., Kawakami, S., Tanaka, M., Ueda, Y., Deguchi, A., Yoshida, J., Yamamoto, Y., Kataoka, F., et al.: Update on GOSAT TANSO-FTS performance, operations, and data products after more than 6 years in space., Atmospheric Measurement Techniques, 9, 2016.

McKeever, J., Durak, B., Gains, D., Jervis, D., Varon, D., Germain, S., and Sloan, J.: GHGSat-D: Greenhouse gas plume imaging and quantification from space using a Fabry-Perot imaging spectrometer, Abstract (A33G-2450) presented at 2017 AGU Fall Meeting, New Orleans, LA, 11–15 December, 2017AGUFM, 2017.

National Academies of Sciences, E. and Medicine: Thriving on Our Changing Planet: A Decadal Strategy for Earth Observation from Space, The National Academies Press, Washington, DC, doi:10.17226/24938, URL https://www.nap.edu/catalog/24938/ thriving-on-our-changing-planet-a-decadal-strategy-for-earth, 2018.

Propp, A. M., Benmergui, J. S., Turner, A. J., and Wofsy, S. C.: MethaneSat: Detecting Methane Emissions in the Barnett Shale Region, in: AGU Fall Meeting Abstracts, 2017.

Rodgers, C. D.: Inverse methods for atmospheric sounding: theory and practice, vol. 2, World scientific, 2000.

Roy, D., Wulder, M., Loveland, T., C.E., W., Allen, R., Anderson, M., Helder, D., Irons, J., Johnson, D., Kennedy, R., Scambos, T., Schaaf, C., Schott, J., Sheng, Y., Vermote, E., Belward, A., Bindschadler, R., Cohen, W., Gao, F., Hipple, J., Hostert, P., Huntington, J., Justice, C., Kilic, A., Kovalskyy, V., Lee, Z., Lymburner, L., Masek, J., McCorkel, J., Shuai, Y., Trezza, R.,

Vogelmann, J., Wynne, R., and Zhu, Z.: Landsat-8: Science and product vision for terrestrial global change research, Remote Sensing of Environment, 145, 154 – 172, doi:https://doi.org/10.1016/j.rse.2014.02.001, URL http://www.sciencedirect.com/science/article/pii/S003442571400042X, 2014.

5 Segl, K., Guanter, L., Rogass, C., Kuester, T., Roessner, S., Kaufmann, H., Sang, B., Mogulsky, V., and Hofer, S.: EeteS—The EnMAP End-to-End Simulation Tool, IEEE Journal of Selected Topics in Applied Earth Observations and Remote Sensing, 5, 522–530, doi:10.1109/JSTARS.2012.2188994, 2012.

Sheng, J.-X., Jacob, D. J., Maasakkers, J. D., Zhang, Y., and Sulprizio, M. P.: Comparative analysis
10 of low-Earth orbit (TROPOMI) and geostationary (GeoCARB, GEO-CAPE) satellite instruments for constraining methane emissions on fine regional scales: application to the Southeast US, Atmospheric Measurement Techniques, 11, 6379–6388, doi:10.5194/ amt-11-6379-2018, URL https://www.atmos-meas-tech.net/11/6379/2018/, 2018.

Thompson, D. R., Thorpe, A. K., Frankenberg, C., Green, R. O., Duren, R., Guanter, L., Hollstein,
15 A., Middleton, E., Ong, L., and Ungar, S.: Space-based remote imaging spectroscopy of the Aliso Canyon CH4 superemitter, Geophysical Research Letters, 43, 6571–6578, doi:10.1002/ 2016GL069079, URL https://agupubs.onlinelibrary.wiley.com/doi/abs/10.1002/ 2016GL069079, 2016.

Thompson, D. R., Natraj, V., Green, R. O., Helmlinger, M. C., Gao, B.-C., and Eastwood,
20 M. L.: Optimal estimation for imaging spectrometer atmospheric correction, Remote Sensing of Environment, 216, 355 – 373, doi:https://doi.org/10.1016/j.rse.2018.07.003, URL http://www.sciencedirect.com/science/article/pii/S0034425718303304, 2018.

Thorpe, A. K., Frankenberg, C., and Roberts, D. A.: Retrieval techniques for airborne imaging of methane concentrations using high spatial and moderate spectral resolution: application to AVIRIS,
25 Atmospheric Measurement Techniques, 7, 491–506, doi:10.5194/amt-7-491-2014, URL https://www.atmos-meas-tech.net/7/491/2014/, 2014.

Thorpe, A. K., Frankenberg, C., Green, R. O., Thompson, D. R., Aubrey, A. D., Mouroulis, P., Eastwood, M. L., and Matheou, G.: The Airborne Methane Plume Spectrometer (AMPS): Quantitative imaging of methane plumes in real time, in: 2016 IEEE Aerospace Conference, pp. 1–
30 14, doi:10.1109/AERO.2016.7500756, 2016.

Thorpe, A. K., Frankenberg, C., Thompson, D. R., Duren, R. M., Aubrey, A. D., Bue, B. D., Green, R. O., Gerilowski, K., Krings, T., Borchardt, J., Kort, E. A., Sweeney, C., Conley, S., Roberts, D. A., and Dennison, P. E.: Airborne DOAS retrievals of methane, carbon dioxide, and water vapor concentrations at high spatial resolution: application to AVIRIS-NG, Atmospheric Measurement
35 Techniques, 10, 3833–3850, doi:10.5194/amt-10-3833-2017, URL https://www.atmos-meas-tech.net/10/3833/2017/, 2017.

Turner, A. J., Jacob, D. J., Wecht, K. J., Maasakkers, J. D., Lundgren, E., Andrews, A. E., Biraud, S. C., Boesch, H., Bowman, K. W., Deutscher, N. M., Dubey, M. K., Griffith, D. W. T., Hase, F., Kuze, A., Notholt, J., Ohyama, H., Parker, R., Payne, V. H., Sussmann, R., Sweeney, C., Velazco, V. A., Warneke, T., Wennberg, P. O., and Wunch, D.: Estimating global and North American methane emissions with high spatial resolution using GOSAT satellite data, Atmospheric Chemistry and Physics, 15, 7049–7069, doi:10.5194/acp-15-7049-2015, URL https://www.atmos-chem-phys.net/15/7049/2015/, 2015.

Turner, A. J., Jacob, D. J., Benmergui, J., Brandman, J., White, L., and Randles, C. A.: Assessing the capability of different satellite observing configurations to resolve the distribution of methane emissions at kilometer scales, Atmospheric Chemistry and Physics, 18, 8265–8278, doi:10.5194/acp-18-8265-2018, URL https://www.atmos-chem-phys.net/ 18/8265/2018/, 2018.

Varon, D., Jacob, D., McKeever, J., Durak, B., and Jervis, D.: Quantifying Methane Emissions from Individual Coal Mine Vents with GHGSat-D Satellite Observations, in: AGU Fall Meeting Abstracts, 2018b.

Varon, D. J., Jacob, D. J., McKeever, J., Jervis, D., Durak, B. O. A., Xia, Y., and Huang, Y.: Quantifying methane point sources from fine-scale satellite observations of atmospheric methane plumes, Atmospheric Measurement Techniques, 11, 5673–5686, doi:10.5194/ amt-11-5673-2018, URL https://www.atmos-meas-tech.net/11/5673/2018/, 2018a.

Xi, X., Natraj, V., Shia, R. L., Luo, M., Zhang, Q., Newman, S., Sander, S. P., and Yung, Y. L.: Simulated retrievals for the remote sensing of CO2, CH4, CO, and H2O from geostationary orbit, Atmospheric Measurement Techniques, 8, 4817–4830, doi:10.5194/amt-8-4817-2015, URL https://www.atmos-meas-tech.net/8/4817/2015/, 2015.

Table 1. Shortwave infrared (SWIR) remote sensors for observing methane point sources

Instrument	Pixel size (km²)	SWIR spectral range (nm)[a]	Spectral resolution (nm)[b]	Signal-to-noise ratio (SNR)[c]	Observing epoch
Aircraft					
AVIRIS-NG[d]	0.003 × 0.003	1600-1700; 2200–2510	5.0	200-400[e]	Campaigns
Satellite					
Atmospheric sensors					
SCIAMACHY[f]	30 × 60	1630–1670	1.4	1500	2002-2012
GOSAT[g]	10 × 10	1630–1700	0.06	300	2009-
GHGSat[h]	0.05 × 0.05	1600–1700	0.1	TBD	2016-
TROPOMI[i]	7 × 7	2305–2385	0.25	100	2017-
AMPS[j]	0.03 × 0.03	1990–2420	1.0	200-400	Proposed
Imaging spectrometers					
PRISMA[k]	0.03 × 0.03	1600-1700; 2200–2500	10	180	2019-
EnMAP[l]	0.03 × 0.03	1600-1700; 2200–2450	10	180	2020-
EMIT[m]	0.06 × 0.06	1600-1700; 2200–2510	7-10	200-300	2022-
SBG[n]	0.03 × 0.03	1600-1700; 2200–2510	7-10	200-300	2025-

[a]Methane has absorption bands near 1650 and 2300 nm.

[b]Spectral resolution is represented by the full-width at half-maximum (FWHM).

[c]For SCIAMACHY and GOSAT, SNR is for CO_2 band used in the CO_2-proxy method retrieval. For other instruments, SNR is at 2300 nm.

[d]Airborne Visible/Infrared Imaging Spectrometer – Next Generation (Thorpe et al., 2017). AVIRIS-NG provides roughly a ground sampling distance (GSD) of 1 m per km altitude. The Frankenberg et al. (2016) and Duren et al. (2019) campaigns operated at 3-4 km altitude.

[e]Along-track oversampling increases SNR by $\sqrt{N}$ where N = number of along-track frames. AVIRIS-NG routinely achieves $N > 4$ so AVIRIS-NG effective SNR at 2300 nm can be as much as 400.

[f]SCanning Imaging Absorption SpectroMeter for Atmospheric CHartographY (Frankenberg et al., 2006)

[g]TANSO-FTS instrument aboard the Greenhouse gases Observing SATellite (Kuze et al., 2016). Pixels are circles of 10 km diameter.

[h]GreenHouse Gases Satellite (McKeever et al., 2017). Revisit times are for selected 12×12 km^2 scenes. The demonstration GHGSat-D instrument presently in space has additional instrument imperfections that limit its precision to 13% (McKeever et al. 2017).

[i]TROPOspheric Monitoring Instrument (Hu et al., 2018)

[j]Airborne Methane Plume Spectrometer (Thorpe et al., 2016)

[k]PRecursore IperSpettrale della Missione Applicativa (http://prisma-i.it)

[l]Environmental Mapping and Analysis Program (Guanter et al., 2015)

[m]Earth Surface Mineral Dust Source Investigation (Green et al., 2018)

[n]Surface Biology and Geology, previously called HyspIRI (Hochberg et al., 2015)
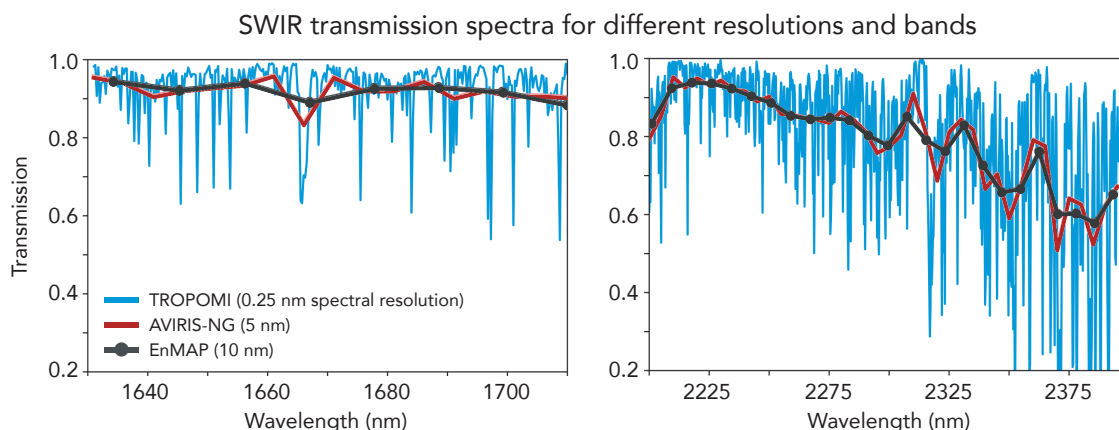
Figure 1. Simulated top of the atmosphere (TOA) transmission spectra for different spectral resolutions (FWHM = full-
width at half-maximum) in the 1650 nm (left panel) and 2300 nm (right panel) shortwave infrared (SWIR) bands. High-
resolution spectra were simulated for the U.S. Standard Atmosphere with 1800 ppb total column methane using the HITRAN
spectroscopic database and the HITRAN Application Programming Interface (HAPI) tool (Kochanov et al., 2016), and were
then sampled with spectral resolutions of 0.25 nm (TROPOMI), 5 nm (AVIRIS-NG), and 10 nm (EnMAP) at the appropriate
wavelength positions.
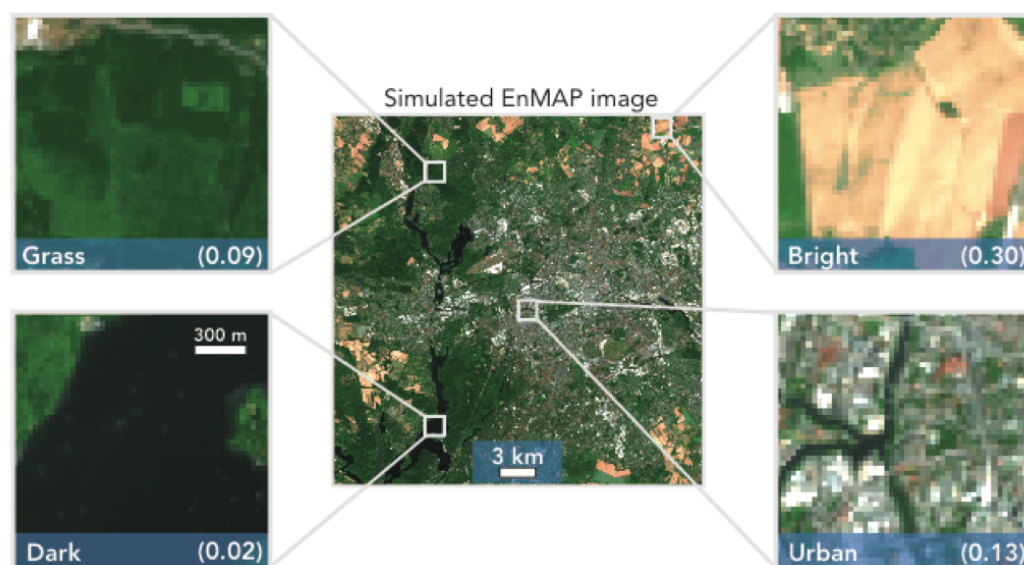
5 **Figure 2**. RGB image of a synthetic EnMAP scene simulated using the EnMAP End-to-End Simulation Tool (EetsS) over Berlin. Four scenes with $30{\times}30$ m^2 pixel resolution are shown (Grass, Dark, Bright, Urban) with average surface reflectances in the SWIR (2210-2410 nm) given in parentheses. These different scenes are used in Section 3 to evaluate the sensitivity of EnMAP to atmospheric methane.
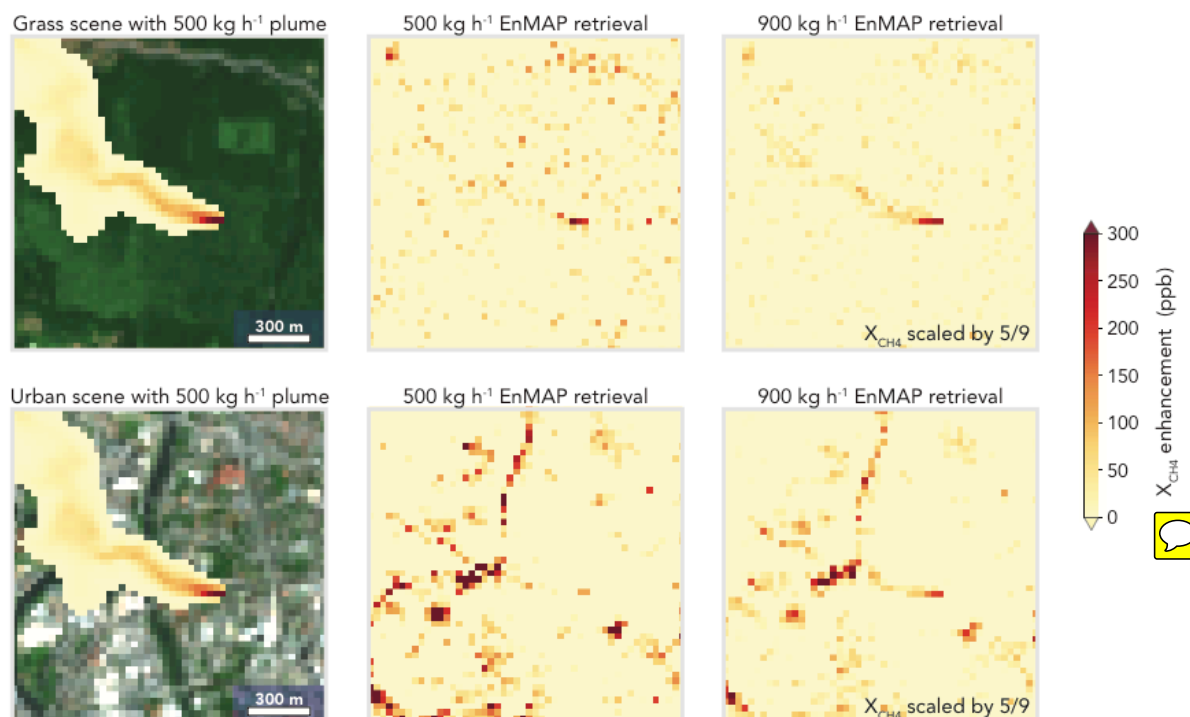
Figure 3. Retrieval of a methane plume over grass and urban EnMAP scenes. The plume was generated by WRF-LES with a source rate of either 500 kg h⁻¹ or 900 kg h⁻¹. The left panels show the dry air column mixing ratio enhancements relative to the 1800 ppb background for a 500 kg h⁻¹ methane plume superimposed on the RGB images of Figure 2. The middle panels show the retrieval of those enhancements using the IMAP-DOAS retrieval algorithm applied to the EnMAP instrument specifications. The right panels show the retrieval of the 900 kg h⁻¹ plume. The X_{CH4} enhancements in the right panels are scaled by 5/9 to be comparable with the other panels. Negative enhancements are reset to equal the background.
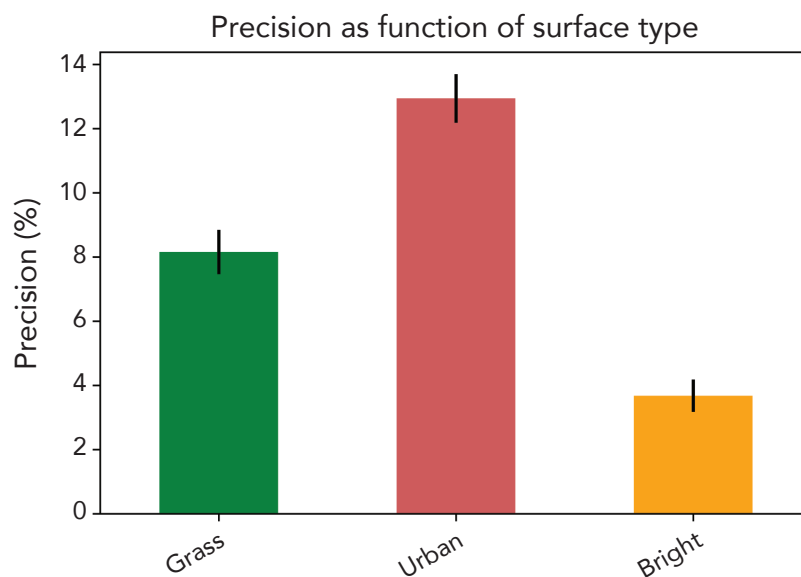
Figure 4. Precision of atmospheric methane retrievals from the EnMAP instrument (Table 1) over different surfaces. The
precisions are the relative root-mean squared errors (RRMSE) between the "true" methane columns in synthetic scenes and
5   values obtained from the IMAP-DOAS retrieval applied to the EnMAP top-of-atmosphere (TOA) backscattered radiances.
The error bars represent the standard deviation over 15 WRF-LES plume realizations and 3 source magnitudes for the plume
(100, 500, 900 kg h^{-1}).
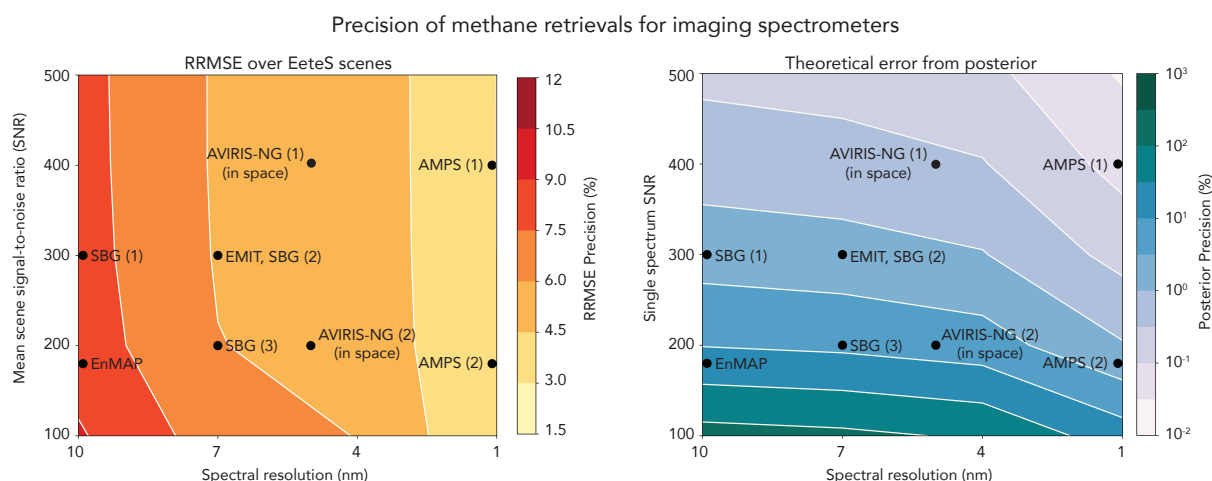
Figure 5. Precision of methane retrievals for spaceborne imaging spectrometers observing in the SWIR (2210-2400 nm), as

5   a function of instrument signal-to-noise (SNR) and full-width half-maximum (FWHM) spectral resolution. The left panel shows precision expressed as the relative root-mean-square error (RRMSE) for synthetic retrievals over three scenes of Figure 2 (Grass, Urban, Bright) including a point source of 100-900 kg h⁻¹ and 15 different WRF-LES plume realizations. The SNR in the left panel represents the mean SNR over all three EeteS scenes. The right panel shows theoretical precision expressed from the posterior error covariance matrix in Equation 7. Black dots show different instrument specifications from

10 Table 1. Specifications for the SBG and AMPS instruments are still at the design stage and values shown here are for the ranges under consideration. Results given for AVIRIS-NG are for a satellite instrument with 30×30 m² pixel resolution, with (1) or without (2) along-track oversampling, and with other specifications (spectral resolution, SNR) the same as the airborne instrument.
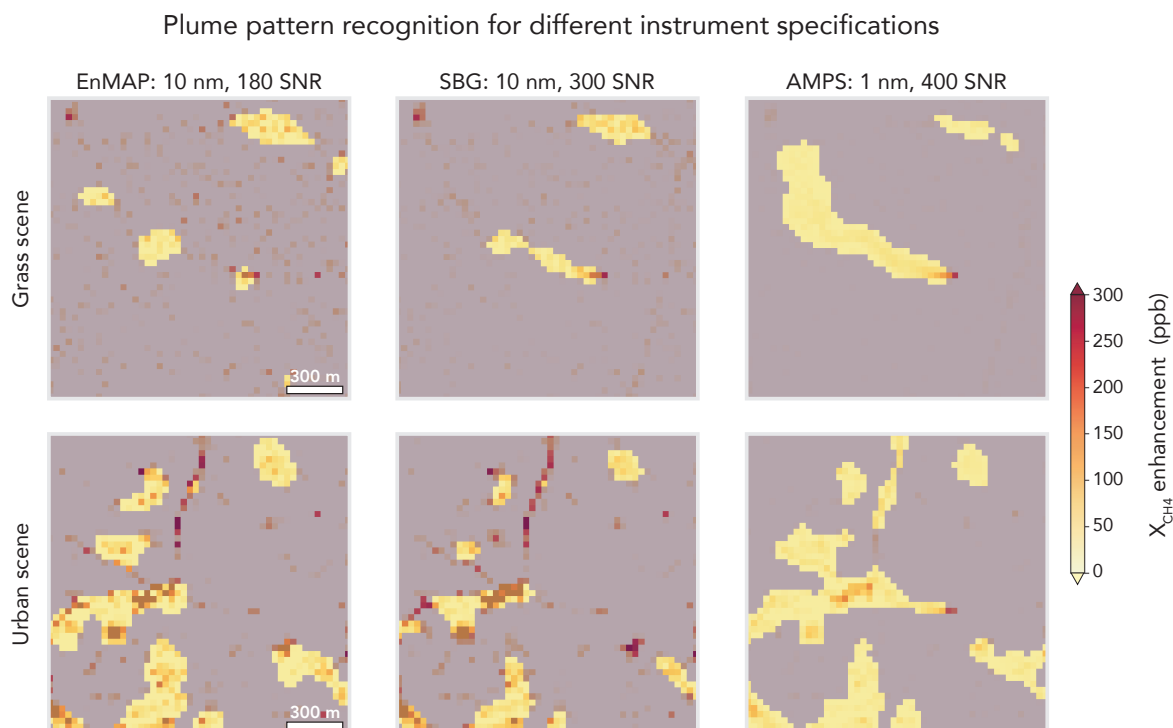
Figure 6. Plume pattern recognition applied to a point source of 500 kg h⁻¹ over Grass and Urban scenes as shown in Figure 3. The plume pattern is defined by applying median and Gaussian filters to pixels above the 80th percentile of X_{CH4} in the scene. Areas excluded by the mask are shown in gray. The panels show retrievals from the EnMAP, SBG, and AMPS instruments.
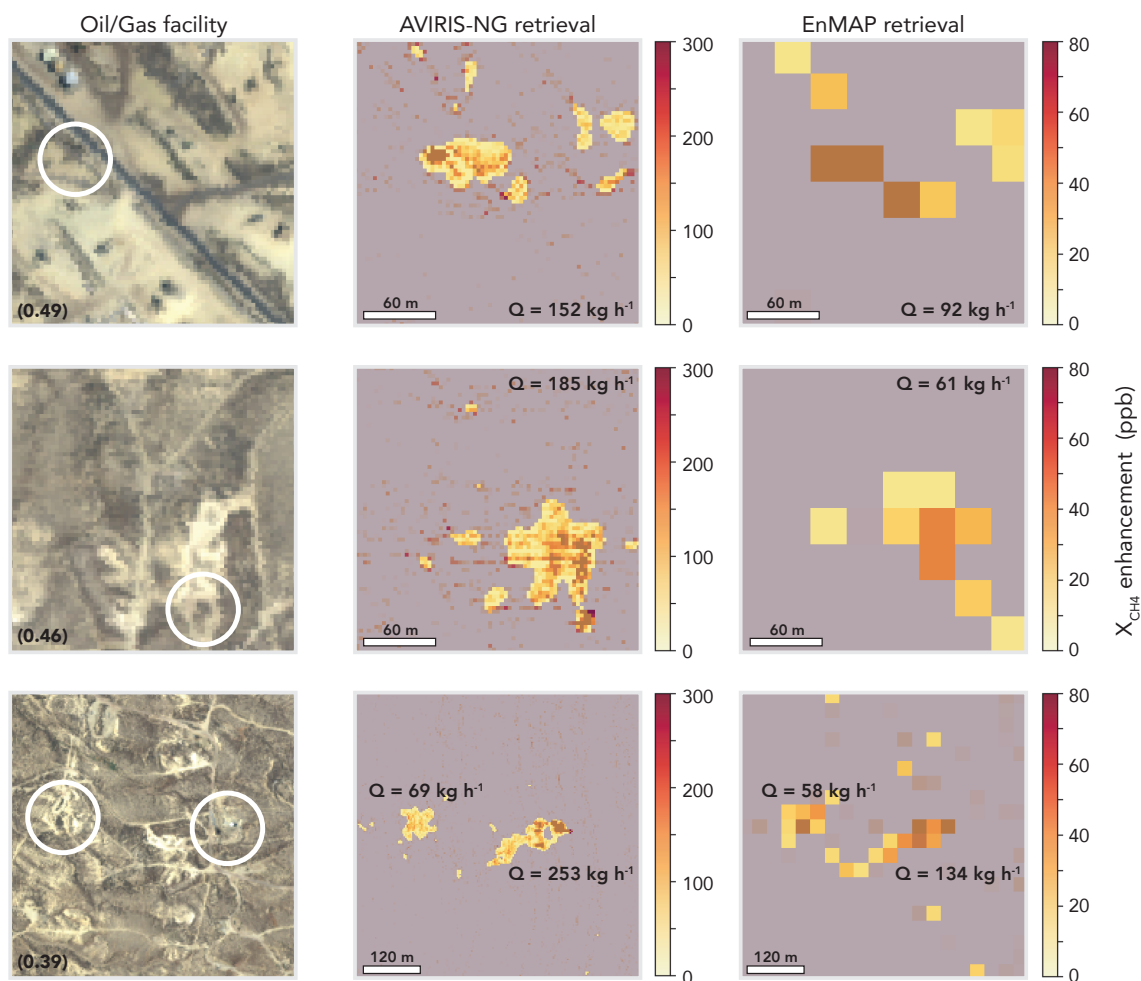
Figure 7. Retrieval of atmospheric methane plumes from oil/gas facilities imaged by the AVIRIS-NG instrument at 3-4 km altitude over California (CARB, 2017). The left panels show the RBG images mapped by AVIRIS-NG with the oil/gas facilities of interest circled. Inset in the bottom left corner is the mean retrieved SWIR surface reflectivity for the scene. The middle panels show the IMAP-DOAS retrieval applied to the AVIRIS-NG images with 3×3 m^2 pixel resolution and 5 nm spectral resolution. The right panels show the IMAP-DOAS retrieval applied to spectra that were spatially and spectrally

downsampled to match EnMAP instrument specifications (30×30 m^2 pixels, 10 nm spectral resolution). Note the difference in color scale for the methane enhancements in the AVIRIS-NG and EnMAP retrievals, reflecting the coarser pixel resolution of EnMAP. The plume mask is overlaid on each. The source rates for each plume obtained from the IME method are inset.